Chapter 3

Quantum chemistry and vibrational spectra

This chapter presents the quantum chemical results for the systems studied in this work, FHF^- (Section 3.2) and OHF^- (Section 3.3). These triatomic anions and their neutral counterparts, FHF and OHF, were assumed to maintain a collinear configuration throughout all calculations. Since bendings were neglected, the molecules retain $C_{\infty v}$ symmetry in all simulations. Furthermore, the anions and their neutral counterparts were assumed to be oriented along a space-fixed Z axis throughout all calculations, unless otherwise noted. Two-dimensional (2D) dipole and potential energy surfaces (PES) were constructed in bond coordinates such that the symmetric and asymmetric normal stretching modes were considered; these results are shown for FHF^- and OHF^- in Sections 3.2.1 and 3.3.1, respectively. In addition to the calculated equilibrium geometries, harmonic and anharmonic vibrational eigenfunctions for FHF^- (Section 3.2.3) and OHF^- (Section 3.3.3) will be discussed and compared to experimental values. In this context, isotope effects will be discussed for FDF^- (Section 3.2.4) and ODF^- (Section 3.3.4). Simulated IR absorption spectra for FHF^- and FDF^- (Section 3.2.5), and for OHF^- and ODF^- (Section 3.3.5), will be presented last.

3.1 Hamiltonian for a linear triatomic molecule

Our goal is to solve first the electronic Schrödinger equation (Eq. (2.4)), for the triatomic anionic systems, FHF^- and OHF^-, and their neutral counterparts, FHF and OHF. Recalling the sums over electrons and nuclei in the exclusively electronic Hamiltonian

(Eq. (2.3)), $M = 3$ since each of these molecules contains three nuclei. For the anion FHF^-, the number of electrons is $N = 20$, building a closed-shell singlet. The neutral FHF is an open-shell doublet with $N = 19$. OHF^- has $N = 19$ so it also builds an open-shell doublet, whereas its neutral counterpart OHF has $N = 18$ and is an open-shell triplet. The electronic Schrödinger equation will be solved for a range of linear nuclear geometries. The nuclear coordinates are the bond distances of the two collinear bonds, $\{\vec{R}_A\} = (R_1, R_2)$. The electronic energies that are obtained at fixed nuclear coordinates will then be used to construct the 2D PES. The electronic problem will be solved using *ab initio* methods that will be described in more detail in Sections 3.2 and 3.3. All *ab initio* calculations were performed using the software program GAUSSIAN 98 [151].

Afterwards, the nuclear Schrödinger equation (Eq. (2.8)) will be solved. Its solution will then deliver the total wave function within the Born-Oppenheimer approximation. The total Hamiltonian operator, consisting of kinetic and potential energy terms, for a triatomic molecule with bond distances R_1 and R_2 is given as,

$$\hat{\mathbf{H}} = \hat{\mathbf{T}}(R_1, R_2) + \hat{\mathbf{V}}(R_1, R_2), \tag{3.1}$$

where the potential energy operator $\hat{\mathbf{V}}$ depends on the nuclear coordinates, (R_1, R_2).

The kinetic energy operator $\hat{\mathbf{T}}(R_1, R_2)$ describes the ro-vibrational (internal) motion of the nuclei $\hat{\mathbf{T}}(R_1, R_2) \equiv \hat{\mathbf{T}}^{\text{internal}}_{nuc}(R_1, R_2)$, and it can be approximated as the sum of two operators, one responsible for vibrational motion and the other for rotational motion (Eq. (2.73)):

$$\hat{\mathbf{T}}^{\text{internal}}_{nuc}(R_1, R_2) \approx \hat{\mathbf{T}}^{\text{vib}}_{nuc}(R_1, R_2) + \hat{\mathbf{T}}^{\text{rot}}_{nuc}(R_1, R_2). \tag{3.2}$$

To calculate the 2D vibrational wave functions and eigenenergies for the linear triatomic molecules, the rotational kinetic energy operator will be neglected. The kinetic energy operator describing the vibrations of the 2D linear system is then given as,

$$\hat{\mathbf{T}}^{\text{vib}}_{nuc}(R_1, R_2) = -\frac{\hbar^2}{2m_1}\frac{\partial^2}{\partial R_1^2} - \frac{\hbar^2}{2m_2}\frac{\partial^2}{\partial R_1^2} - \cos\gamma\frac{\hbar^2}{m_{\text{H}}}\frac{\partial}{\partial R_1}\frac{\partial}{\partial R_2} \tag{3.3}$$

where γ is the internal bond angle ($\gamma = 180°$ for collinear geometries), and m_1 and m_2 are reduced masses,

$$m_{\text{X}} = \frac{m_{\text{X}} m_{\text{H}}}{m_{\text{X}} + m_{\text{H}}}, \qquad \text{X} = \text{F}, \text{O}. \tag{3.4}$$

The case of a vibrating and rotating molecule will not be treated in this thesis. However, in the case of OHF^-, rotational wave functions will be calculated within the rigid rotor approximation in Section 4.4.1. In the application to follow, the total angular momentum $J = R + L + S$ consists of nuclear angular momentum R due to the orbiting rigid body and electronic orbital angular momentum L; the spin angular momentum, $S = 1/2$, will be neglected. The electronic contribution $L = 1$ is considered small compared to the total

angular momentum J. Therefore, J can be considered to consist predominantly of nuclear angular momentum, $J \approx R$ and the total kinetic energy operator is then

$$\hat{\mathbf{T}}_{nuc}^{\mathrm{rot}} \approx B\hat{\mathbf{J}}^2 \qquad \text{(rigid rotor)} \tag{3.5}$$

where B is the rotational constant and $\hat{\mathbf{J}}^2$ is the total angular momentum operator squared, introduced in Section 2.5.1, *i.e.* $\hat{\mathbf{T}}_{nuc}^{\mathrm{rot}}$ is equivalent to $\hat{\mathbf{H}}_{r.r.}$ from Eq. (2.200).

Next, in Section 3.2, the solutions of the electronic and nuclear Schrödinger equations for FHF^- will be discussed. In Section 3.3, the electronic and nuclear problem will be treated for OHF^-.

3.2 FHF^-/FHF

The geometry optimization of FHF^-, as well as calculations of harmonic vibrational frequencies, was performed using the quadratic configurational interaction method, including single and double excitations (QCISD) [105], with Dunning's polarized valence correlation consistent (cc)[1] triple-split basis set *d*-aug-cc-pVTZ [152]. Due to the delocalized negative charge of the anion in the $^1\Sigma$ ground state, doubly-augmented diffuse functions are required for H and F. Anharmonic vibrational frequencies are estimated from the calculated QCISD 2D potential energy surface. The more economic QCSID method was chosen in view of the quantitative agreement with CCSD(T) calculations of FHF^- [71], that had demonstrated good agreement with experiment [78].

3.2.1 Potential energy and dipole surfaces

The nuclear coordinates $\{\vec{R}_A\}$ consist of the collinear bond distances between $F_a - H$ and $F_b - H$ and are labelled $R_1(\equiv F_a - H)$ and $R_2(\equiv F_b - H)$. For the construction of the 2D PES for the closed-shell singlet FHF^- ($^1\Sigma$) and open-shell doublet FHF ($^2\Sigma$), the coordinates R_1 and R_2 were each varied from 0.6 to 3.0 Å over 16 grid points along one dimension, making a total of $136(=16(16+1)/2)$ *ab initio* single energy points. Taking advantage of the symmetry of the molecule, we obtained a square PES of $256(\equiv 16^2)$ *ab initio* data points for each surface. From the 256 *ab initio* points, a grid of $\mathcal{N} = 8192$ ($\equiv 64 \times 128$) points was constructed using a bi-cubic spline, as implemented in the program *qmbound* [119].

The PES for the anion and neutral are shown in Figure 3.1. The PES for the anion contains a local minimum energy at $R_1 = R_2 = 1.141$ Å (marked with •). The PES corresponding to the neutral surface is dissociative, with a transition state located at $R_1 = R_2 = 1.141$ Å (marked with •), and with two equivalent dissociation channels leading to identical chemical products, F + HF. The vertical energy spacing between the minimum energy of FHF^- and the transition state of FHF (at the geometry $R_1 = R_2 = 1.141$ Å) is 6.1 eV, shown schematically in Figure 3.2. The FHF^- anion is tightly bound with respect to the products HF + F^-, with a binding energy of 1.9 eV, or 43.8 kcal/mol. This binding energy is in close agreement with CCSD(T) binding energy of 44.6 kcal/mol [71]. Experimentally, the binding energy in the gas phase has been

[1] Correlation consistent (cc) basis sets consist of shells of functions added to a core set of atomic Hartree-Fock functions. These added functions contribute correlation energy to the atomic calculation which, typically, only applies to valence electrons.

measured to be 38.6 kcal/mol [73] and $\geq$ 34.6 kcal/mol [76]. The neutral species FHF is dissociative, with a calculated exothermicity of 0.3 eV, or 6.9 kcal/mol. To the best of our knowledge, no experimental data pertaining to the energy profile of the neutral PES is available for comparison.

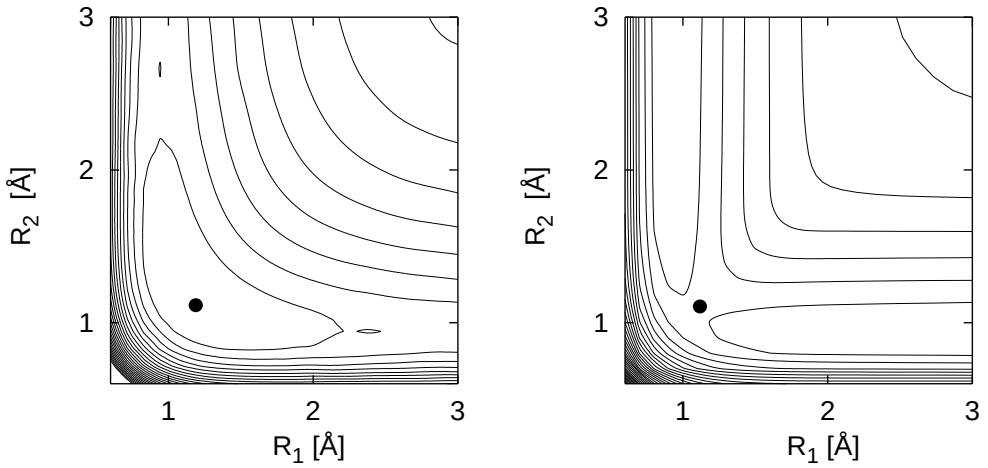

Figure 3.1: 2D potential energy surfaces for FHF^- (left) and FHF (right). A local minimum in the anionic PES and a transition state in the neutral PES (both marked with •) are located at $R_1 = R_2 =$ 1.141 Å. Equidistant contours ($\Delta E = 1.0$ eV) of the energies are relative to the global FHF^- minimum energy.

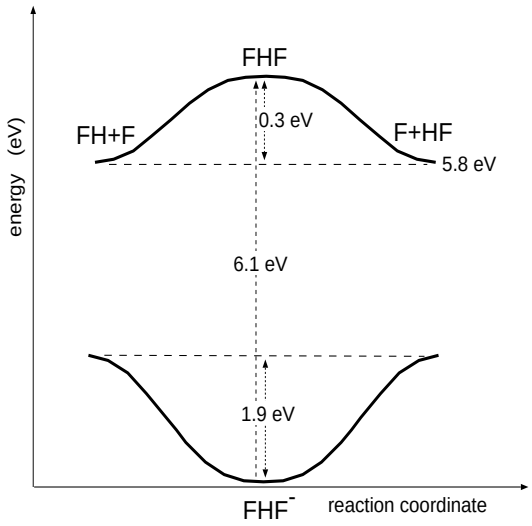

Figure 3.2: Schematic FHF^- and FHF potential energy (eV) profile along the reaction coordinate F +HF $\leftrightarrow$ FH + F. The minimum energy of FHF^- and the transition state of FHF are located at $R_1 = R_2 = 1.141$ Å.

Permanent dipole values for FHF^- were also calculated at the QCISD level of theory, and the 2D dipole surface is shown in Figure 3.3. Similar to the PESs, the permanent dipole surface also contains a line of symmetry at $R_1 = R_2$, dividing—in this case—values of opposite sign (solid vs. dashed lines in Figure 3.3). In the case of FHF^-, due to the molecule's net charge of -1, the dipole moment depends on the frame of reference of electron and nuclear coordinates [67]. As a result, the permanent dipole moment must be computed with respect to its instantaneous center of mass [67].

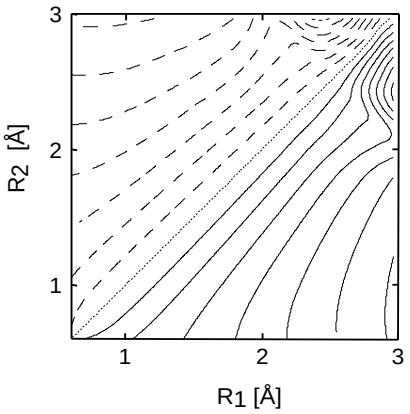

Figure 3.3: 2D permanent dipole moment surface for FHF^-. Solid vs. dashed lines correspond to values of opposite sign. Equidistant contours ($\Delta\mu_0 = 1.0$ Debye) of the dipole values are relative to the value $\mu_0 = 0$ Debye at the line $R_1 = R_2$.

The transition dipole moment that couples the PESs corresponding to anionic and neutral species has been set to 1 within the Condon approximation [121]. In this approximation, the transition dipole moment is assumed to be independent of the nuclear coordinates [121]. For a more detailed discussion of estimating ionic-to-neutral transition dipole moments beyond the Condon approximation, see Ref. [153]. The permanent dipole moment of the neutral surface was set equal to 0. As a result, vibrational excitations within the PES of neutral FHF were not considered.

3.2.2 Geometry optimization and rotational constant

The harmonic QCISD and CCSD(T) F–F bond lengths, along with the computed anharmonic QCISD and CCSD(T) values, and the experimental value, are listed in Table 3.1. Anharmonic F–F bond lengths are calculated from the expectation values of the F—H bond length, $\langle R_{FH} \rangle$, allowing for averaging over features of the entire ground state wave function. The harmonic QCISD length is calculated to be 2.273 Å, within 99% of both the harmonic CCSD(T) value of 2.282 Å [71], as well as the experimental value of 2.278 Å [78]. The anharmonic QCISD F–F distance, 2.326 Å , and anharmonic CCSD(T) F–F distance, 2.316 Å , are both larger than the harmonic values, as expected,

Table 3.1: QCISD and CCSD(T), and experimental equilibrium F–F bond lengths

F–F [Å]	**harmonic**		**anharmonic**		**experiment**
	QCISD	CCSD(T)[a]	QCISD	CCSD(T)[a]	gas[b]
			$\langle R_{HF} \rangle$		
FHF^-	2.273	2.282	2.326	2.316	2.278
			$\langle R_{DF} \rangle$		
FDF^-	—	—	2.318	2.310	2.295[c]

[a]CCSD(T) [71]
[b]gas phase [78]
[c]gas phase [154]

due to averaging over the ground state wave function.

The rotational constant B of FHF^- could also be obtained from the geometry optimization. The computed QCISD rotational constant, as well as the value calculated from the expression $B = \hbar/2I$, where I is the moment of inertia (calculated according to Eq. (2.207), see Appendix A for a complete discussion of the calculation of the moment of inertia) at the equilibrium bond lengths of $R_1 = 1.141$ Å and $R_2 = 1.141$ Å, are listed in Table 3.2. The QCISD and calculated values[2] are identical, 0.341 cm^{-1}. The experimental value, measured in the gas phase to be 0.342 cm^{-1} [78], within 99% of the QCISD and calculated values.

Table 3.2: QCISD, calculated, and experimental FHF^- rotational constant

	QCISD	$\boldsymbol{B = \hbar/2I}$	**experiment**[a]
B **[cm^{-1}]**	0.341	0.341	0.342

[a]gas phase [78]

[2]Energies and frequencies will be listed in this chapter with the units cm^{-1}. One should note that the unit cm^{-1} is an inverse wavelength (λ^{-1}) and is related to frequency through $\nu = \frac{c}{\lambda}$, where c is the speed of light and λ is the wavelength. The wavelength is related to energy, $E = h\nu$, through $E = \frac{hc}{\lambda}$.

3.2.3 Eigenenergies and vibrational frequencies

From the 2D anionic PES, low-lying symmetric and asymmetric anharmonic eigenfunctions were calculated for FHF^- using the Fourier Grid Hamiltonian (FGH) method (see Section 2.3.5) [112, 113]. Twelve low-lying eigenfunctions and their eigenenergies obtained using the FGH on this square grid are shown in Figure 3.4. (A complete list of the lowest twenty-six ($\Psi_0 - \Psi_{25}$) eigenfunctions is given in Appendix B). The notation of eigenfunctions Ψ^v will be simplified now to just $v_{s\,as}$, where s and as refer to symmetric and asymmetric modes, respectively. $v_{s\,0}$ and $v_{0\,as}$ correspond to pure symmetric and asymmetric stretching modes, respectively, whereas $v_{s\,as}$ corresponds to mixed-modes. The symmetric functions contain nodes perpendicular to the line of symmetry, $R_1 = R_2$, whereas the asymmetric functions contain nodal planes parallel to the line $R_1 = R_2$.

The spacings between the lowest pure-mode vibrational eigenstates, $v_{10} \leftarrow v_{00} = 593$ cm^{-1} and $v_{01} \leftarrow v_{00} = 1448$ cm^{-1}, correspond to the fundamental symmetric ν_1 and asymmetric ν_3 vibrational frequencies, respectively. The bending vibration, ν_2, can not be obtained from the 2D eigenfunctions. These anharmonic vibrational frequencies are listed in Table 3.3, along with anharmonic values from CCSD(T) calculations [71], harmonic CCSD(T) and QCISD values, and results from gas phase microwave experiments [78] and solid-phase experiments [155, 156, 157] for comparison. The gas phase experiments were performed using diode laser spectroscopy [78]. The solid phase experiments consisted of either IR [156] or Raman [157] spectra taken of crystalline KHF_2, or FHF^- in a cold (12 K), inert argon matrix [155]. The experimental values can be regarded as exact "3D" reference values, although discrepancies between these experimental values may arise due to the various media in which the spectra were recorded.

The value of the symmetric stretching frequency, $\nu_1 (\equiv v_{10} \leftarrow v_{00}) = 593$ cm^{-1}, agrees with the experimental value of 583 cm^{-1} to within 98%, and with the CCSD(T) value of 595 cm^{-1} to within 99%. As expected, the anharmonic values are all lower than the nearly identical harmonic QCISD and CCSD(T) frequencies, 649 cm^{-1} and 640 cm^{-1}, respectively. The first and second excited QCISD symmetric stretching frequencies can be calculated from the transition $v_{20} \leftarrow v_{10}$ and $v_{30} \leftarrow v_{20}$ (see Figure 3.4) and are found to be 584 cm^{-1} and 578 cm^{-1}, respectively; both are smaller than the fundamental transition ($\equiv v_{10} \leftarrow v_{00}$). This decrease in energy spacing is expected from the anharmonic model.

Larger deviations are seen between the values of the asymmetric stretching frequencies. The QCISD asymmetric stretching frequency, $\nu_3 = 1448$ cm^{-1} is 117 cm^{-1} higher than the experimentally measured gas phase value of 1331 cm^{-1}, an agreement

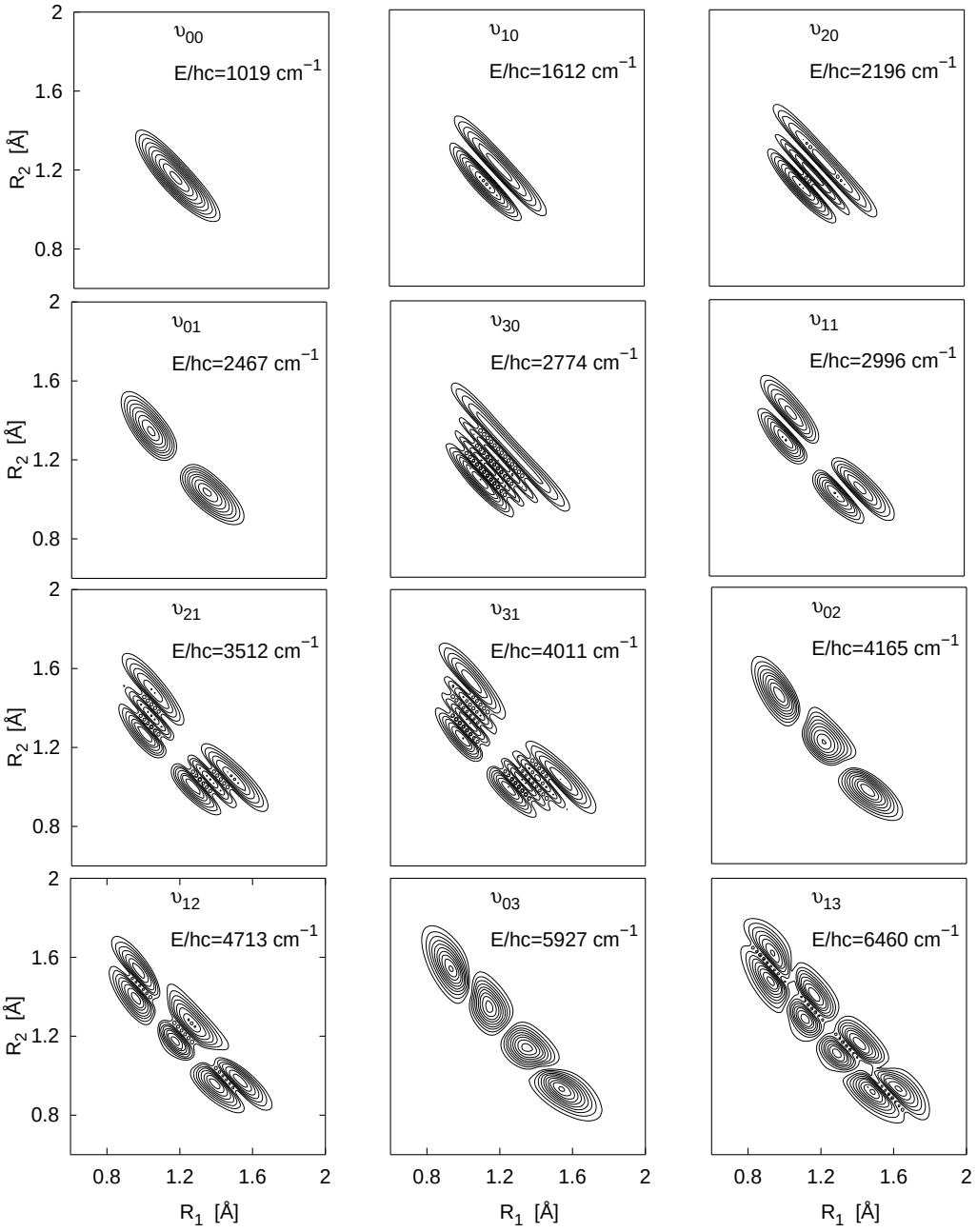

Figure 3.4: 2D anharmonic vibrational eigenfunctions for FHF$^-$, labelled $\upsilon_{s\,as}$. The symmetric functions ($\upsilon_{s\,0}$) contain nodes perpendicular to the line of symmetry, $R_1 = R_2$, whereas the asymmetric ($\upsilon_{0\,as}$) functions contain nodal planes parallel to the line $R_1 = R_2$. Mixed-mode functions ($\upsilon_{s\,as}$) contain nodes both parallel and perpendicular to the line $R_1 = R_2$. Contours correspond to wave packet density.

of $\sim$92%, and 71 cm^{-1} higher than the value obtained in a solid Ar matrix, 1377 cm^{-1}, demonstrating agreement of $\sim$ 95%. The QCISD value is 28 cm^{-1} lower than the CCSD(T) value, an agreement of 98%. The large deviation of the QCISD and CCSD(T)

Table 3.3: Calculated QCISD, CCSD(T), and experimental vibrational frequencies of FHF^-.

FHF^-		**experiment**		**harmonic**		**anharmonic**	
		gas[a]	solid[b]	QCISD	CCSD(T)[c]	QCISD	CCSD(T)[c]
Frequency [cm^{-1}]							
ν_1 (sym)	$\equiv v_{10} \leftarrow v_{00}$	583*	600[e]	649	640	593	595
	$v_{20} \leftarrow v_{10}$					584	585
	$v_{30} \leftarrow v_{20}$					578	573
ν_2 (bend)		1286	$1225-1275$[e]	1380	1347	—	—
ν_3 (asym)	$\equiv v_{01} \leftarrow v_{00}$	1331	1377	1250	1244	1448	1476
	$v_{02} \leftarrow v_{01}$					1698	
	$v_{03} \leftarrow v_{02}$					1762	
$(2\nu_1)$	$\equiv v_{20} \leftarrow v_{00}$					1177	
$(3\nu_1)$	$\equiv v_{30} \leftarrow v_{00}$					1755	
$(\nu_1+\nu_3)$	$\equiv v_{11} \leftarrow v_{00}$	1849	2044			1977	2007
$(2\nu_1+\nu_3)$	$\equiv v_{21} \leftarrow v_{00}$		2602			2493	2525
$(3\nu_1+\nu_3)$	$\equiv v_{31} \leftarrow v_{00}$		3166			2992	
$(2\nu_3)$	$\equiv v_{02} \leftarrow v_{00}$					3146	
$(\nu_1+2\nu_3)$	$\equiv v_{12} \leftarrow v_{00}$					3694	
$(3\nu_3)$	$\equiv v_{03} \leftarrow v_{00}$		5090			4908	
$(\nu_1+3\nu_3)$	$\equiv v_{13} \leftarrow v_{00}$		5643			5441	

[a] gas phase [78]

[b] IR spectrum of crystalline KHF_2 [156]

[c] CCSD(T) [71]

[d] solid Ar matrix [155]

[e] Raman spectrum of crystalline KHF_2 [157]

* Since the frequency of the symmetric stretching band (ν_1) is not directly observable experimentally, this frequency is often estimated by subtracting the fundamental frequency of the asymmetric stretch, (ν_3), from that of the combination band ($\nu_1+\nu_3 \equiv v_{11} \leftarrow v_{00}$), which is observed experimentally.

values from the experimental frequency is largely due to the neglect in the 2D theoretical treatment of the bending-stretching coupling via Coriolis perturbations [67]. The comparable values of the experimental bending frequency, $\nu_2 = 1286$ cm^{-1}, and the asymmetric stretching frequency $\nu_3 = 1331$ cm^{-1}, indicate that mixing of these modes could be significant and should be taken into account for a more accurate description of the frequencies. Unlike the symmetric stretching frequencies, the asymmetric (QCISD and CCSD(T)), stretching frequencies are significantly *higher* than the harmonic values,

1250 (QCISD) and 1244 (CCSD(T)) cm^{-1}. The experimental value 1331 cm^{-1}, lies in the middle of the harmonic and anharmonic values. These discrepancies indicate both the inadequacy of the harmonic approximation as well as the lack of mode-mixing in the 2D model. Inverse harmonicity can also be seen in the spacing between the QCISD asymmetric stretch eigenfunctions (see Table 3.3); the frequency spacing between vibrational levels increases from $1448(\equiv \upsilon_{01} \leftarrow \upsilon_{00})$ cm^{-1} to $1698(\equiv \upsilon_{02} \leftarrow \upsilon_{01})$ cm^{-1} and to $1762(\equiv \upsilon_{03} \leftarrow \upsilon_{02})$ cm^{-1}. Extending the 2D model to include the bending vibration would allow for more relaxation of the wave function and would most likely lead to closer agreement with the experimental value of ν_3.

The QCISD energy of the combination band $\nu_1 + \nu_3(\equiv \upsilon_{11} \leftarrow \upsilon_{00}) = 1977$ cm^{-1}, involving one quantum each of symmetric and asymmetric vibrations, is within 99% of the CCSD(T) value of 2007 cm^{-1} and 97% of the experimental value 2044 cm^{-1} obtained in solid KHF_2 [156]. The combination band $\nu_1 + \nu_3$ calculated in the gas phase is the lowest, at $= 1849$ cm^{-1}, and is within 94% of the QCISD value. The mixed-mode $2\nu_1 + \nu_3(\equiv \upsilon_{21} \leftarrow \upsilon_{00}) = 2493$ cm^{-1} is also within 99% of the CCSD(T) value of 2525 cm^{-1} and within 96% of the value 2602 cm^{-1}, obtained in solid KHF_2 [156]. The mode involving three quanta of symmetric stretching vibrations and one mode of asymmetric vibration, $3\nu_1 + \nu_3(\equiv \upsilon_{31} \leftarrow \upsilon_{00})$, was calculated to be 2992 cm^{-1}, within 95% of the solid KHF_2 value, while the QCISD values $3\nu_3 = 4908$ cm^{-1} and $\nu_1 + 3\nu_3 = 5441$ cm^{-1} are both within 96% of the solid KHF_2 values of 5090 cm^{-1} and 5643 cm^{-1}, respectively.

3.2.4 Isotope effects: FDF^-

Isotope effects on equilibrium bond lengths and vibrational eigenfunctions were examined by calculating QCISD vibrational eigenfunctions of FDF^-. Due to the lower zero-point energy of the heavier isotopomer, the F–D bond length is expected to be shorter than the F–H bond length. Indeed, the anharmonic QCISD value for $\langle R_{DF} \rangle$ is 2.318 Å, compared to 2.326 Å for $\langle R_{HF} \rangle$, and in 99% agreement with the anharmonic CCSD(T) value of $\langle R_{DF} \rangle = 2.310$ Å. The QCISD and calculated rotational constant for FDF^- are the same as for FHF^-, $B = 0.332$ cm^{-1} (see Table 3.2), since the moment of inertia is the same for the symmetric molecules. The experimental value of the rotational constant, obtained in the gas phase [77], is $B = 0.333$ cm^{-1}.

Twelve low-lying pure and mixed-mode eigenfunctions and their energies are shown in Figure 3.5. The symmetric and asymmetric stretching frequencies, along with CCSD(T) [71] and experimental values [77, 78, 156, 157] are listed in Table 3.4 for comparison. The fundamental and first two excited symmetric stretching frequencies of

FDF^-, $\nu_1 = 598(\equiv \upsilon_{10} \leftarrow \upsilon_{00})$ cm^{-1}, $587(\equiv \upsilon_{20} \leftarrow \upsilon_{10})$ cm^{-1}, and $570(\equiv \upsilon_{30} \leftarrow \upsilon_{20})$ cm^{-1} are nearly identical to those of FHF^-, as expected for the vibration of the heavy atoms. The spacing between these levels also decreases slightly due to the anharmonic model. These values are also within 99% of the CCSD(T) values of $601(\equiv \upsilon_{10} \leftarrow \upsilon_{00})$ cm^{-1}, $588(\equiv \upsilon_{20} \leftarrow \upsilon_{10})$ cm^{-1}, and $570(\equiv \upsilon_{30} \leftarrow \upsilon_{20})$ cm^{-1}, respectively [71]. The asymmetric stretching frequencies, however, $\nu_3 = 1002(\equiv \upsilon_{01} \leftarrow \upsilon_{00})$ cm^{-1}, $1163(\equiv \upsilon_{02} \leftarrow \upsilon_{01})$ cm^{-1}, and $1197(\equiv \upsilon_{03} \leftarrow \upsilon_{02})$ cm^{-1}, are approximately 500 cm^{-1} lower than the corresponding frequencies of FHF^-, due to the larger mass of deuterium. As a result, the eigenstate υ_{01} lies lower in energy than the state υ_{20}, unlike in the case of FHF^- (*cf.* Figure 3.4). The FDF^- value of ν_3, 1002 cm^{-1}, agrees to within 96% of the experimental value, 965 cm^{-1}, obtained for FDF^- in a solid argon matrix [155], and agrees to within 93% of the gas phase value of 934 cm^{-1} [77]. The QCISD value agrees within 98% of the theoretical CCSD(T) value 1023 cm^{-1}.

Interestingly, the lowest anharmonic QCISD values for the symmetric stretching frequency of FDF^-, 598 and 587 cm^{-1}, are slightly higher than the corresponding values for FHF^-, 593 and 584 cm^{-1}, respectively (*cf.* Table 3.3). The same trend is observed for the CCSD(T) values. Typically, the eigenfunctions of the heavier isotopomer are expected to lie deeper than those of the lighter isotopomer. The experimental (Raman) values available for comparison of ν_1 are almost identical, *i.e.* $\nu_1 = 600$ cm^{-1} for FHF^- and $\nu_1 = 601$ cm^{-1} for FDF^- [157]. The reverse behavior of the eigenenergies in the 2D anharmonic models (QCISD and CCSD(T)) indicates that a 3D model may be necessary to allow for relaxation of the wave function in the PES.

Table 3.4: Calculated QCISD, CCSD(T), and experimental vibrational frequencies of FDF^-.

FDF^-		**experiment**		**harmonic**	**anharmonic**	
		gas[a]	solid[b]	QCISD	QCISD	CCSD(T)[c]
Frequency [cm^{-1}]						
ν_1 (sym)	$\equiv v_{10} \leftarrow v_{00}$		601[e]	649	598	601
	$v_{20} \leftarrow v_{10}$				587	588
	$v_{30} \leftarrow v_{20}$				570	570
ν_2 (bend)			$884 - 907$[d]	989	—	—
ν_3 (asym)	$\equiv v_{01} \leftarrow v_{00}$	934	965[e]	896	1002	1023
			$995 - 1023$[d]			
	$v_{02} \leftarrow v_{01}$				1163	1176
	$v_{03} \leftarrow v_{02}$				1197	
$(2\nu_1)$	$\equiv v_{20} \leftarrow v_{00}$				1185	
$(\nu_1 + \nu_3)$	$\equiv v_{11} \leftarrow v_{00}$	1469	1597		1546	1569
$(3\nu_1)$	$\equiv v_{30} \leftarrow v_{00}$				1755	
$(2\nu_1 + \nu_3)$	$\equiv v_{21} \leftarrow v_{00}$		2070		2071	2100
$(2\nu_3)$	$\equiv v_{02} \leftarrow v_{00}$				2165	
$(\nu_1 + 2\nu_3)$	$\equiv v_{12} \leftarrow v_{00}$				2713	
$(3\nu_1 + \nu_3)$	$\equiv v_{31} \leftarrow v_{00}$		2519		2880	2614
$(3\nu_3)$	$\equiv v_{03} \leftarrow v_{00}$		3561		3662	
$(\nu_1 + 3\nu_3)$	$\equiv v_{13} \leftarrow v_{00}$				4217	

[a] gas phase [78]
[b] IR spectrum of crystalline KDF_2 [156]
[c] CCSD(T) [71]
[d] solid Ar matrix [155]
[e] Raman spectrum of crystalline KDF_2 [157]

Similar to the inverse anharmonicity observed in FHF^-, the spacing between the asymmetric stretching vibrational levels for FDF^- also increases, from $1002(\equiv v_{01} \leftarrow v_{00})$ cm^{-1} to $1163(\equiv v_{02} \leftarrow v_{01})$ cm^{-1} and to $1197(\equiv v_{03} \leftarrow v_{02})$ cm^{-1}. The symmetric stretching vibration, corresponding to the motion of the heavy end atoms, therefore follows expected anharmonic behavior, whereas the oscillation of the light hydrogen atom between the heavy end atoms (asymmetric stretch) resembles a particle-in-a-box model, whose energy levels are spaced increasingly farther apart. The QCISD value of the combination band $\nu_1 + \nu_3(\equiv v_{11} \leftarrow v_{00})$ was calculated to be 1546 cm^{-1}, within 99% of the CCSD(T) value of 1569 cm^{-1} and within 97% and 95% of the solid KHF_2 and gas phase values, respectively. The mixed-mode $2\nu_1 + \nu_3(\equiv v_{21} \leftarrow v_{00})$ was calculated to be 2071 cm^{-1},

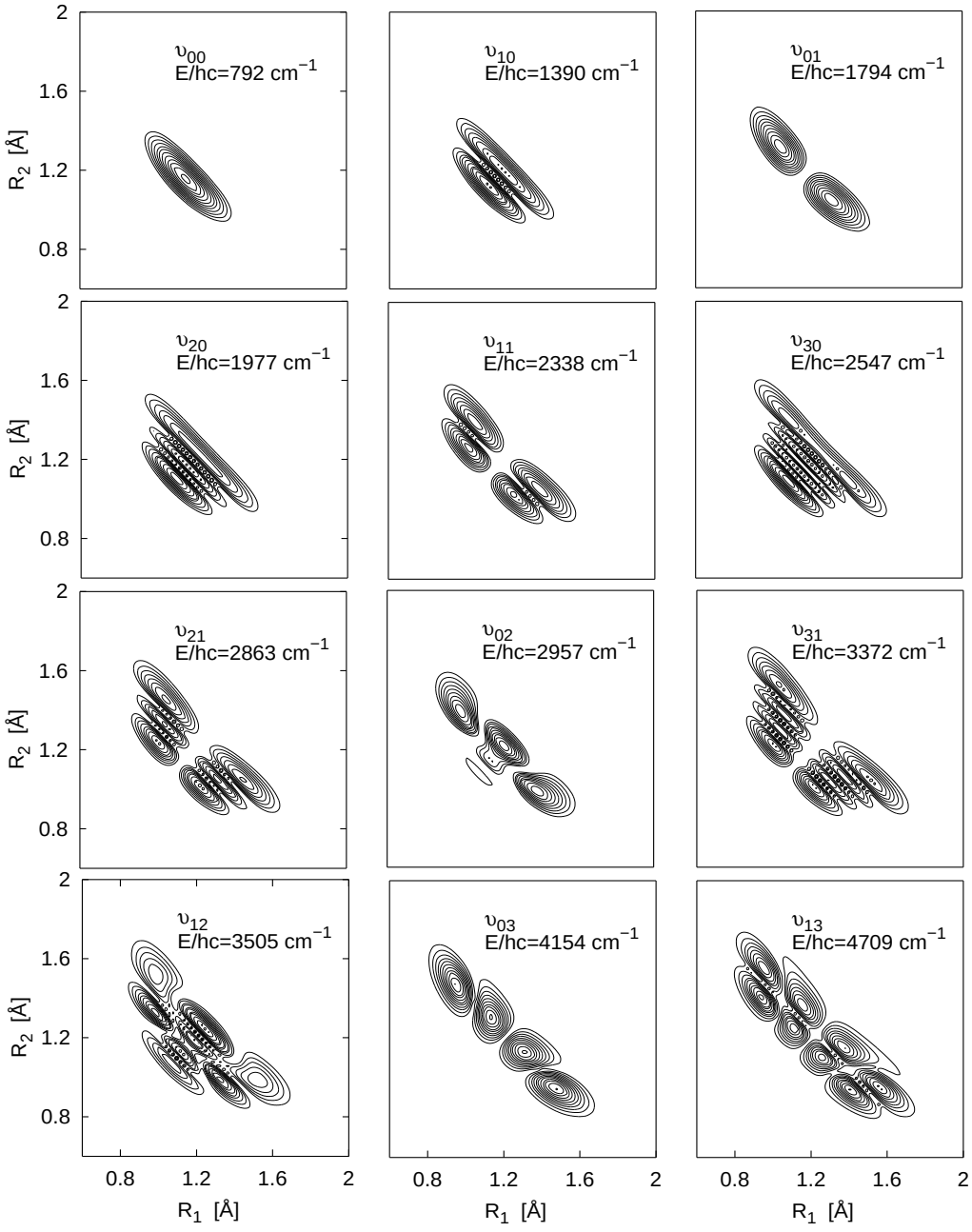

Figure 3.5: 2D anharmonic vibrational eigenfunctions for FDF^-, labelled $\upsilon_{s\,as}$. The symmetric functions ($\upsilon_{s\,0}$) contain nodes perpendicular to the line of symmetry, $R_1 = R_2$, whereas the asymmetric ($\upsilon_{0\,as}$) functions contain nodal planes parallel to the line $R_1 = R_2$. Mixed-mode functions ($\upsilon_{s\,as}$) contain nodes both parallel and perpendicular to the line $R_1 = R_2$. Contours correspond to wave packet density.

in 99% agreement with both the CCSD(T) value of 2100 cm^{-1} as well as the solid KHF_2 value of 2070 cm^{-1}. The QCISD value of $3\nu_1 + \nu_3 (\equiv \upsilon_{31} \leftarrow \upsilon_{00})$ is calculated to be 2880 cm^{-1}, in 91% agreement with the CCSD(T) value of 2614 cm^{-1} and 87%

agreement with the value of 2519 cm^{-1}, obtained from an IR spectrum of solid KHF_2 [156].

Knowing the asymmetric stretching vibrations of FHF^- and FDF^-, we can introduce a "scaling" factor, which we will denote b, that relates the frequencies of the two isotopomers through the ratio of masses. The reduced mass involved in the asymmetric stretching vibration ν_3 is given as

$$\mu_{as}(FZF^-) = \frac{m_Z\, 2m_F}{m_Z + 2m_F} \approx m_Z \tag{3.6}$$

for Z = H or D. Since both isotopomers have the same force constant, k_{as}, one can write

$$k_{as} = \mu_{as}(FHF^-)\nu_3(FHF^-)^2 = \mu_{as}(FDF^-)\nu_3(FDF^-)^2. \tag{3.7}$$

This relationship implies that the scaling factor b is just the ratio between the two asymmetric stretching frequencies,

$$b \approx \sqrt{\frac{\mu_{as}(FDF^-)}{\mu_{as}(FHF^-)}} \approx \sqrt{\frac{m_D}{m_H}} \approx \frac{\nu_3(FDF^-)}{\nu_3(FHF^-)}. \tag{3.8}$$

A comparison of these values is shown in Table 3.5. The agreement between the scaling

Table 3.5: The scaling factor b for isotopomers FHF^- and FDF^- calculated using the mass of the isomers (m), the reduced mass of the asymmetric stretching vibration (μ_{as}), and the asymmetric stretching frequency, (ν_3).

	scaling factor (b)			
$\sqrt{(m_D)/(m_H)}$	1.41			
$\sqrt{(\mu_{as}(FDF^-)/(\mu_{as}(FHF^-))}$	1.40			
	gas[a]	solid[b]	QCISD	CCSD(T)[c]
$\nu_3(FHF^-)/\nu_3(FDF^-)$	1.43	1.43	1.45	1.44

[a]gas phase [78]
[b]solid Ar matrix [155]
[c]CCSD(T) [71]

factor of the reduced masses and that of the anharmonic asymmetric stretching vibrations is, expectedly, quite close for the gas phase [78] and solid [155] values of 1.43, which are

both 99% of the QCISD value of 1.45 and 99% of the CCSD(T) value 1.44 [71]. Later, in Section 4.3.6, the scaling factor will be revisited in the discussion of designing few-cycle IR laser pulses to drive the asymmetric stretching vibration of the heavy isotopomer, FDF^-.

3.2.5 IR absorption spectra of FHF^- and FDF^-

For a final comparison of the two isotopomers, simulated IR absorption spectra for FHF^- and FDF^- are shown in Figure 3.6; peak locations and relative intensities are listed in Table 3.6. The absorption spectra were obtained using the method described

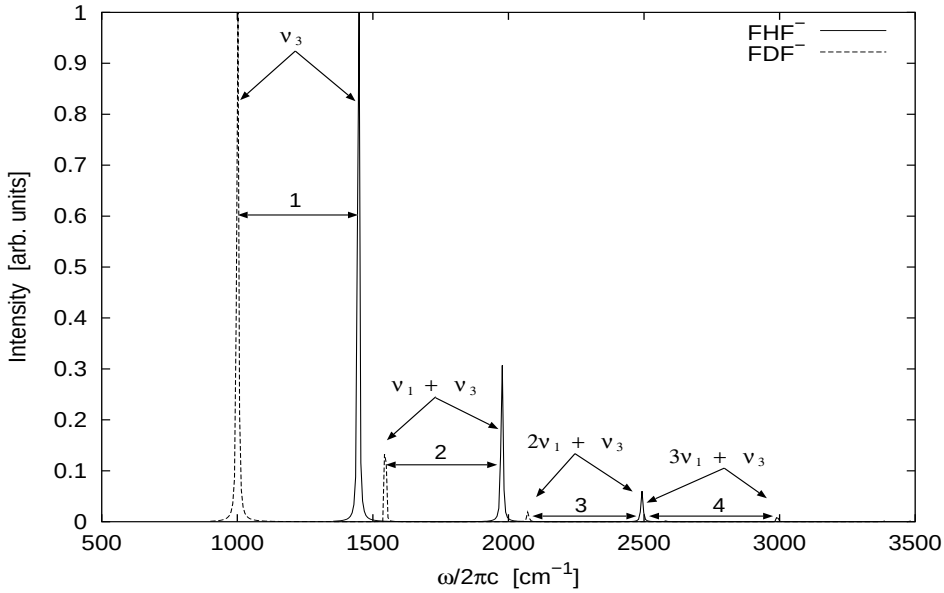

Figure 3.6: Absorption spectra of FHF^- (solid lines) and FDF^- (dashed lines). Vibrational transitions are indicated. Separations between peaks corresponding to the two isotopomers are labelled (1), (2), (3), and (4).

in Section 2.3.4, in which the Fourier transform of the permanent dipole autocorrelation function is calculated (see Eq. (2.149)); propagations were carried out for 5 ps. The solid peaks correspond to FHF^-, and the dashed peaks correspond to FDF^-. The frequencies at which the peaks occur can be correlated to transitions between pure and mixed-mode vibrational states. One should note that peaks due to pure symmetric stretching vibrations are absent from the spectrum since these modes are IR-inactive.

The peaks of highest intensity (1.00), at 1002 cm^{-1} (dashed) and 1449 cm^{-1} (solid), correspond to the transition from the ground state to the lowest asymmetric stretching vibration, $\upsilon_{01} \leftarrow \upsilon_{00}$, of FDF^- and FHF^-, respectively.

Table 3.6: Frequencies and relative intensities of FHF^- and FDF^- IR absorption peaks obtained from the theoretical calculation and experiment.

Transition [cm^{-1}]	**FHF^-**				**FDF^-**			
	Calculation		Experiment		Calculation		Experiment	
	Freq.	Int.	Freq.	Int.	Freq.	Int.	Freq.	Int.
$\nu_3(\equiv v_{01} \leftarrow v_{00})$	1449	1.0	1331[a] 1377[b]		1002	1.0	934[a] 965[b] 969[c]	
$\nu_1 + \nu_3(\equiv v_{11} \leftarrow v_{00})$	1977	0.31	1849[a]		1543	0.13		
$2\nu_1 + \nu_3(\equiv v_{21} \leftarrow v_{00})$	2492	0.06			2071	0.02		
$3\nu_1 + \nu_3(\equiv v_{31} \leftarrow v_{00})$	2989	<0.01			2580	<0.01		
$(\nu_1 + \nu_3) - \nu_3$ *	528 531[d]	— —	516[a]	—	541 546[d]	— —		

[a]gas phase [78]
[b]solid Ar matrix [155]
[c]solid Ar matrix [91]
[d]anharmonic CCSD(T) [90]
* Since the frequency of the symmetric stretching band (ν_1) is not directly observable experimentally, this frequency is often estimated by subtracting the fundamental frequency of the asymmetric stretch, (ν_3), from that of the combination band ($\nu_1 + \nu_3 \equiv v_{11} \leftarrow v_{00}$), which is observed experimentally.

Less probable are transitions from the ground state to mixed-modes, and these peaks accordingly have lower relative intensities: for FDF^- at 1543 cm^{-1} with intensity of 0.13 (dashed) and for FHF^- at 1977 cm^{-1} with intensity 0.31 (solid), the peaks belong to the $v_{11} \leftarrow v_{00}$ transition. The relative intensity of the ν_3 band with respect to the combination band $\nu_3 + \nu_1$ is therefore 3.1 : 1 for FHF^-, and 7.7 : 1 for FDF^-. A gas phase spectrum of FHF^-, recorded by Kawaguchi *et al.*, indicates that the relative intensities of the $\nu_3 : \nu_3 + \nu_1$ bands are on the order of 4 : 1 [77]. Kawaguchi *et al.* also observed that, in general, the peaks corresponding to FDF^- were several time weaker in intensity than those of FHF^- [77].

The peaks at 2071 cm^{-1} with 0.02 intensity (dashed) for FDF^- and for FHF^- at 2492 cm^{-1} with 0.06 intensity (solid), are due to the $\upsilon_{21} \leftarrow \upsilon_{00}$ transition. The peaks with weakest relative intensities (< 0.01), for FHF^- at 2989 cm^{-1} and for FDF^- at 2580 cm^{-1} (overlapping in Figure 3.6 with the peak located at 2492 cm^{-1}), correspond to the transition to the mixed-mode $\upsilon_{31} \leftarrow \upsilon_{00}$ with three quanta of symmetric stretching vibration and one quantum of asymmetric stretching vibration. Agreement with the frequencies obtained from the QCSID eigenfunctions is excellent for all visible peaks.

Although the frequency of the fundamental symmetric stretching vibration, ν_1, is not observed in the spectrum, it can be extracted from the difference of the combination band $(\nu_1 + \nu_3)$ and ν_3, *i.e.* $[(\nu_1 + \nu_3) - \nu_3]$, both of which are observable. From the simulated absorption spectrum, this difference for FHF^- is calculated to be 528 cm^{-1} (*cf.* Table 3.6), in 99% agreement with the CCSD(T) value 531 cm^{-1} [71], and 97% agreement with the value obtained in gas phase experiment, 516 cm^{-1} [78]. For FDF^-, the frequency difference $[(\nu_1 + \nu_3) - \nu_3]$ obtained from the simulated spectrum is 541 cm^{-1}, 13 cm^{-1} higher than that of FHF^- and within 99% agreement of the CCSD(T) value of 546 cm^{-1} [71]. This increased frequency, compared to FHF^- at 528 cm^{-1}, is due to the relatively smaller contribution from the asymmetric stretching vibration of FDF^- (1002 cm^{-1} for FHF^- versus 1449 cm^{-1} for FDF^-) due to the heavier mass of deuterium. The resulting difference $[(\nu_1 + \nu_3) - \nu_3]$ is accordingly higher for FDF^- than for FHF^-

The separation between peaks belonging to one isotopomer is nearly constant, and it corresponds to quanta of symmetric stretching that separate the peaks υ_{01}, υ_{11}, υ_{21}, and υ_{31}. The first peak separation $(\overset{1}{\leftrightarrow})$ is 447 cm^{-1}; the ratio of the frequencies of these isotopomer peaks corresponding to the same vibration (asymmetric stretch, $\nu_3 = \upsilon_{01} \leftarrow \upsilon_{00}$) is $b = 1.45$, as expected from the calculated ratios listed in listed in Table 3.5. For the peak separations $(\overset{2}{\leftrightarrow})$, $(\overset{3}{\leftrightarrow})$, and $(\overset{4}{\leftrightarrow})$, this separation between isotopomer frequencies decreases slightly to 434 cm^{-1}, 421 cm^{-1}, and finally 409 cm^{-1}, due to anharmonicity.

In general, experimentally measured frequencies are lower than the simulated ones, most likely since the real "3D" model allows for complete relaxation of the wave function. For example, for FHF^-, the calculated value of ν_3 is 1449 cm^{-1}, whereas the experimental value is 1331 cm^{-1}; for FDF^-, $\nu_3 = 1002$ cm^{-1} and the gas phase value is 934 cm^{-1}.

3.3 OHF/OHF$^-$

The most recent theoretical investigation of $OHF^-(^2\Pi)$ and $OHF(^3\Pi)$ used a complete active space (CASSCF) procedure for subsequent multireference configuration interaction (MRCI) calculations to generate a high quality three-dimensional (3D) PES for the electronic ground state [94]. This study of the neutral surface point to the absence of a barrier to the reaction $OH(^2\Pi) + F(^2P) \rightarrow O(^3P) + HF(^1\Sigma^+)$. Earlier work constructed the PESs using unrestricted second and fourth order Møller-Plesset perturbation theory, UMP2 and UMP4 respectively, and then fit an analytical function to the *ab initio* data at very short and very long ranges [83, 93]. These data were in good agreement with the MRCI results. With knowledge of the accuracy of the less demanding UMP4 surfaces, we chose to optimize the geometry of OHF^-, and to construct our 2D *ab initio* potential energy and permanent dipole surfaces for OHF^- and OHF, at this level of theory. Similar to our treatment of FHF^-, simulations of OHF^- were only performed for a collinear geometry, so bendings were neglected. Unfortunately, no experimental data to our knowledge is available for comparison, so the followling discussion will only contain references to other theoretical studies of OHF^- and OHF.

3.3.1 Potential energy and dipole surfaces

In our calculations, the standard 6-31++G(d,p) basis set was used for the ground state of the open-shell doublet anion, $^2\Pi$, and the triplet neutral, $^3\Pi$, including diffuse functions located at the heavy atoms and hydrogen (++) to describe the anionic character, as well as polarization functions for both the heavy atoms and hydrogen (d,p). The nuclear coordinates $\{\vec{R}_A\}$ consisted of the collinear bond distances between O–H and H–F and are denoted R_{OH} and R_{HF}. To construct the 2D PES, the bonds R_{OH} and R_{HF} were varied in steps of 0.1 Å, from 0.6 to 3.0 Å, and from 0.6 to 4.0 Å, respectively. A total of 850 *ab initio* single point energies were calculated for the anion and neutral PESs, and the same number of permanent dipole values were calculated for the anion. Next, one-dimensional (1D) cuts were taken along the R_{OH} and R_{HF} coordinates, and a 1D cubic spline routine [158] was implemented to smooth and extend the curves, for R_{OH} from 3.0 Å to 4.0 Å, and for R_{HF} from 4.0 Å to 5.0 Å; a total of 918 points was obtained. The extension of the grid was performed to provide enough surface for the dissociative wave packet dynamics simulations. For the calculation of eigenfunctions, a grid of $\mathcal{N}=8192$ ($\equiv 64 \times 128$) points was constructed from the 918 data points using a bi-cubic spline, as implemented in *qmbound* [119]. The coordinate R_{OH} is described with 128 grid points, while the R_{HF} coordinate is discretized in 64 grid intervals.

The 2D anion and neutral PES are shown in Figure 3.7. Unlike the PESs of FHF^- and FHF, the surfaces of OHF^- and OHF are asymmetric. The anionic PES

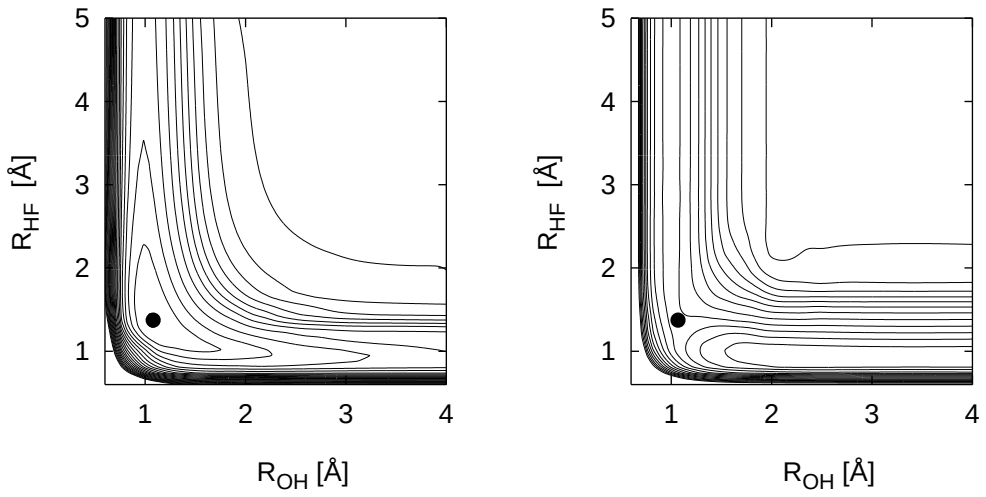

Figure 3.7: Potential energy surfaces for OHF^- (left) and OHF (right). A minimum in the anionic PES (marked with •) is located at $R_{OH} = 1.07$ and $R_{HF} = 1.38$ Å. The neutral PES contains a transition state (marked with •) at $R_{OH} = 1.10$ Å and $R_{HF} = 1.45$ Å. Equidistant energy contours ($\Delta E = 0.5$ eV) are relative to the global OHF^- minimum energy.

(Figure 3.7, left) contains a local minimum (marked with •) at $R_{OH} = 1.07$ Å and $R_{HF} = 1.38$ Å. The neutral PES (Figure 3.7, right) is unbound, with a transition state (marked with •) located at $R_{OH} = 1.10$ Å and $R_{HF} = 1.45$ Å, and dissociation products OH + F and O + FH. One should note that the contours of the neutral PES indicate a significant slope in the direction of the products O + HF. Indeed, previous investigations of the OHF dissociation dynamics indicated that the topology of the neutral PES heavily favors the products O + HF, with a branching ratio of 0.7 : 0.3 with respect to the products OH + F [93]. Let us now examine the potential energy profile along the reaction coordinate O +HF $\leftrightarrow$ OH + F for the anion and neutral species in more detail.

Previous UMP2 investigations of the 2D PES of OHF^- by Bradforth *et al.* predicted that the products OH + F^- and O^- + HF lie 1.48 eV and 2.05 eV higher, respectively, than the minimum energy at the geometry $R_{OH} = 1.08$ Å and $R_{HF} = 1.35$ Å [83]. Bradforth *et al.* also concluded that the barrier height 12 kcal/mol of the neutral reaction OH + F $\rightarrow$ O + HF, calculated by Sloan *et al.* [92], was overestimated. Based on experimental photo-electron spectra, Bradforth *et al.* estimated its value to lie within $2 - 9$ kcal/mol

(0.09 − 0.39 eV) [83]; they assumed that the location of the barrier, as calculated in Ref. [92], R_{OH}=1.08 Å and R_{HF}=1.32 Å, was correct. A more recent investigation by Gómez-Carrasco *et al.* places the barrier to the neutral reaction OH + F → O + HF at R_{OH}=1.46 Å and R_{HF}=1.02 Å, albeit for a bent geometry, with an angle of $\gamma = 109°$ [94]. Dixon *et al.*—who used an analytical fit to extrapolate *ab initio* UMP4 energy values at short (< 0.8 Å) and long ranges (> 4.0 Å)—calculated the saddle point and OH + F products of the neutral species OHF($^3\Pi$) to lie 1.90 eV and 1.47 eV above the energy of the O + HF products, respectively [93].

In Figure 3.8, a sketch of our calculated UMP4 potential energy profile for OHF$^-$ and OHF is shown. On the anionic potential energy curve, the products OH + F$^-$ and O$^-$ + HF lie 1.49 eV and 2.80 eV higher than the minimum, respectively. The minimum UMP4 energy of the anion is located at the geometry $R_{OH} = 1.07$ Å and $R_{HF} = 1.38$ Å.

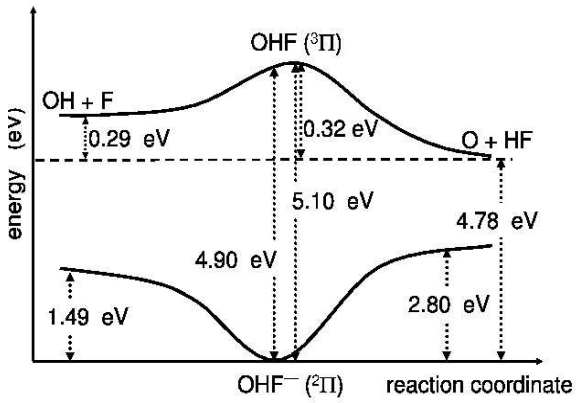

Figure 3.8: Schematic OHF$^-$ and OHF potential energy (eV) profile along reaction coordinate O +HF ↔ OH + F. The minimum energy of OHF$^-$ is located at $R_{OH} = 1.07$ Å and $R_{HF} = 1.38$ Å, and the transition state of OHF is located at R_{OH}=1.10 Å and R_{HF}=1.45 Å.

The energy of the neutral system at the minimum geometry is 4.90 eV. The transition state in the neutral PES is located at a slightly different geometry, namely R_{OH}=1.10 Å and $R_{HF} = 1.45$ Å, and the potential energy of OHF at the transition state is 5.10 eV. On the neutral PES, the barrier to the reaction OH + F → O + HF is calculated to be (0.32 − 0.29) = 0.03 eV (0.7 kcal/mol), smaller than the range predicted by Bradforth *et al.*, 0.09 − 0.39 eV [83]. The energy difference between the OH + F products and O + HF products is 0.29 eV, smaller than the value 1.47 eV calculated by Dixon *et al.* Similarly, our barrier height of 0.32 eV to the reaction OH + F → O + HF is also more than 1 eV smaller than the value 1.90 eV calculated by Dixon *et al.* These discrepancies in energy values could be due to the analytical fitting procedure used by Dixon *et al.* to obtain asymptotic potential energy values of the neutral OHF. The dissociation products OH + F and O + HF are located 5.07(= 4.78 + 0.29) eV and 4.78 eV higher than the

minimum energy of the anion OHF^-, respectively.

A similar asymmetry in dissociation channels can be seen in the 2D permanent dipole moment surface of OHF^-, shown in Figure 3.9. As in the case of FHF^-, due to the net charge of OHF^- of -1, the permanent dipole moment has been calculated with respect to its center of mass. A high density of contours near $R_{OH} > 2$ Å, and

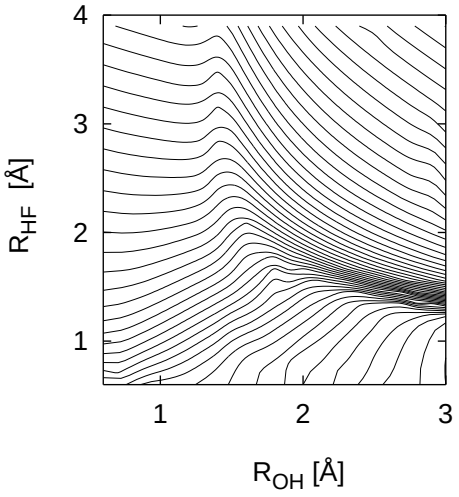

Figure 3.9: 2D permanent dipole moment surface for OHF^-. Equidistant contours ($\Delta\mu_0 = 0.5$ Debye) of the dipole values are relative to the value $\mu_0 = 0.01$ Debye at the equilibrium geometry, $R_{OH} = 1.07$ and $R_{HF} = 1.38$ Å.

$R_{HF} < 2$ Å suggests a steep surface in this region. Later, during wave packet simulations, we will see how the topology of both the PES and the permanent dipole surface strongly drives the reaction toward the O + HF exit channel. Similar to the case of FHF^-, the transition dipole moment that couples the anionic and neutral PESs, was set to 1 within the Condon approximation [121]. Also, the permanent dipole of the neutral system was set equal to 0, so vibrational transitions within the neutral PES were not considered in the forthcoming wave packet dynamics simulations.

3.3.2 Geometry optimization and rotational constant

Table 3.7 contains the computed F—H and O—H equilibrium bond lengths. Harmonic UMP4 geometry optimizations of collinear OHF^- yield an O—H bond length of 1.07 Å and an F—H bond length of 1.38 Å. These bond length values are in good agreement with previous harmonic UMP2 results that calculated an O—H bond length of 1.08 Å and an F—H bond length of 1.35 Å, agreement of 99% and 98%, respectively [83]. 3D MRCI/CASSCF calculations also confirmed the UMP4 results with an estimated

Table 3.7: 2D harmonic UMP4 and UMP2, 3D MRCI, and 2D anharmonic UMP4 O–H and F–H equilibrium bond lengths

OHF$^-$ bond lengths [Å]	**harmonic**			**anharmonic**	
	UMP4	UMP2[a]	MRCI[b]	UMP4	
					ODF$^-$
				$\langle R_{OH} \rangle$	$\langle R_{OD} \rangle$
O–H	1.07	1.08	1.08	1.12	0.85
				$\langle R_{FH} \rangle$	$\langle R_{FD} \rangle$
F–H	1.38	1.35	1.32	1.26	1.10

[a]UMP2 [83]
[b]3D MRCI [95]

$R_{OH} = 1.08$ Å and $R_{HF} = 1.32$ Å [95]. Anharmonic O–H and F–H bond lengths were calculated in the same manner as described for FHF$^-$ (*cf.* Section 3.2), namely by computing the expectation values $\langle R_{OH} \rangle$ and $\langle R_{FH} \rangle$ over the entire anharmonic UMP4 ground state wave function. These calculated values, $R_{OH} = 1.12$ Å and $R_{HF} = 1.26$ Å, differ slightly from the harmonic values. In particular, the anharmonic R_{OH} is larger than the harmonic values, demonstrating agreement within 96% of the harmonic values, 1.04 Å (UMP4), 1.08 Å (UMP2 [83] and MRCI [94]). The anharmonic R_{HF} agrees to within 91% of the harmonic value of 1.38 Å. Discrepancies between the anharmonic UMP4 values and the harmonic and anharmonic MRCI values can arise due to the shallow nature of the anion PES, which causes spreading of the wave function. Averaging the wave function over the entire grid may therefore lead to deviations from the geometry observed near the minimum, or the equilibrium bond lengths. Let us now turn our attention to the vibrational eigenfunctions and eigenenergies of OHF$^-$, as obtained from the 2D anionic PES.

From the UMP4 geometry optimization, the rotational constant B of OHF$^-$ could also be obtained. The computed UMP4 rotational constant, as well as the value calculated from the expression $B = \hbar/2I$, where I is the moment of inertia (calculated according to Eq. (2.207), see Appendix A for a complete discussion of the calculation of the moment of inertia) at the equilibrium bond lengths of $R_{OH} = 1.07$ Å and $R_{HF} = 1.38$ Å, are listed in Table 3.8. The calculated value 0.323 cm^{-1} is within 98% of the UMP4 value of 0.328 cm^{-1}. The value $B = 0.33$ cm^{-1} will be used in the simulations of rotational wave packets in Section 4.4.1. To our knowledge, no experimental value is

available for comparison.

Table 3.8: UMP4 and calculated OHF^- rotational constant

	UMP4	$\boldsymbol{B = \hbar/2I}$
B $[\mathbf{cm}^{-1}]$	0.328	0.323

3.3.3 Eigenenergies and vibrational frequencies

Anharmonic 2D vibrational eigenstates (υ_{sas}) and eigenenergies for OHF^- were obtained from the 2D PES, using the Fourier Grid Hamiltonian (FGH) method (see Section 2.3.5) [112, 113]. Twelve low-lying states are depicted in Figure 3.10, and the corresponding eigenenergies are also listed in Table 3.9, along with 2D UMP4 values, anharmonic UMP2 values [83], and 3D MRCI values [94], for comparison. (A complete list of the lowest twenty-six ($\Psi_0 - \Psi_{25}$) eigenfunctions is given in Appendix B). The 3D MRCI model consisted of stretching and bending vibrations, defined in Jacobi coordinates [95]. These coordinates, as defined in Ref. [95], consist of the HF internuclear distance, r_{HF}, the distance between the HF center of mass and the O atom, R_{O-HF}, and the angle between these two vectors, γ_{rR}. The motion of the HF center of mass with respect to the O atom, R_{O-HF}, can be considered roughly analogous to the 2D symmetric stretching vibration (ν_1) of the heavy end atoms, and the motion of H and F, described by the coordinate r_{HF}, can be compared to the asymmetric stretching vibration (ν_3). UMP2 frequencies [83] were obtained in a similar set of coordinates, namely considering a fixed R_{OF} distance and then the vibration along the coordinate R_{OH}. A Morse potential was then fit along the R_{OH} coordinate at the equilibrium R_{OF} geometry of $1.08 + 1.35 = 2.43$ Å, and the UMP2 asymmetric stretching wave functions were calculated. In the following discussion, we will compare our calculated frequencies with the results of these studies, although discrepancies may arise due to the different treatments of the coordinate system. In general, however, a 3D model should provide a better description of the system since relaxation of the wave function along all normal modes is possible. Nonetheless, experimental data would be required for a definitive comparison.

The anharmonic value of the symmetric stretching vibration, obtained from the vibrational eigenfunctions, $496 (= \upsilon_{10} \leftarrow \upsilon_{00})$ cm^{-1}, is 19 cm^{-1} higher than the harmonic

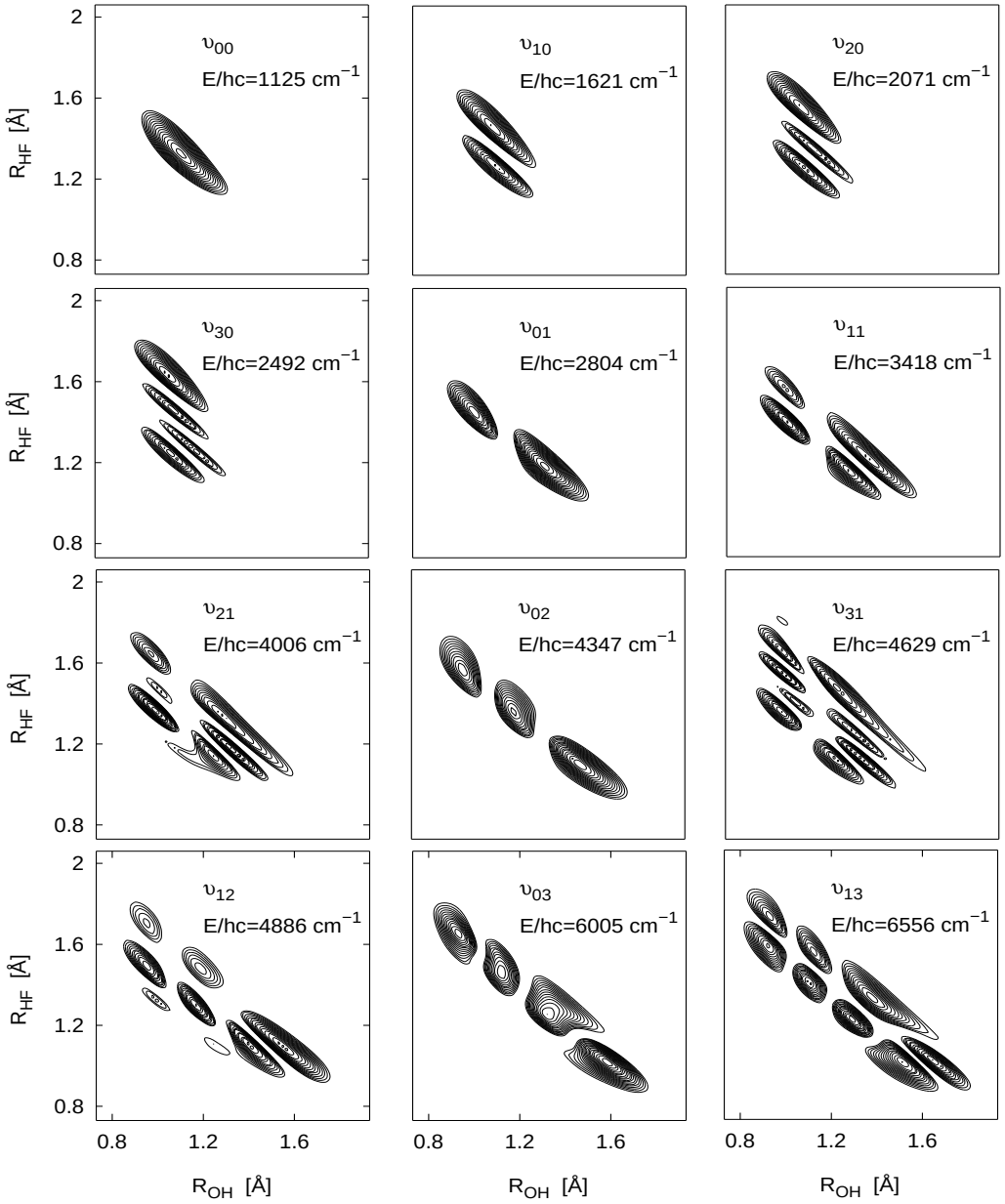

Figure 3.10: 2D anharmonic vibrational eigenfunctions for OHF$^-$, labelled $\upsilon_{s\,as}$. The symmetric functions ($\upsilon_{s\,0}$) contain nodes perpendicular to the line $R_1 = R_2$, whereas the asymmetric ($\upsilon_{0\,as}$) functions contain nodal planes parallel to the line $R_1 = R_2$. Mixed-mode functions ($\upsilon_{s\,as}$) contain nodes both parallel and perpendicular to the line $R_1 = R_2$. Contours correspond to wave packet density.

UMP4 symmetric stretching frequency, 477 cm^{-1} and it is 63 cm^{-1} higher than the anharmonic UMP2 value of 433 cm^{-1}, agreement of 87%. The anharmonic value 496 cm^{-1} agrees to 99% of the MRCI value of 500 cm^{-1} [95].

Table 3.9: 2D harmonic UMP4, 2D anharmonic UMP2 and UMP4, and 3D MRCI vibrational frequencies of OHF^-

OHF^-		**harmonic**	**anharmonic**		
		UMP4	UMP2[a]	UMP4	MRCI[b]
Frequency [cm^{-1}]					
ν_1 (sym)	$\equiv v_{10} \leftarrow v_{00}$	477	433	496	500
	$v_{20} \leftarrow v_{10}$			450	
	$v_{30} \leftarrow v_{20}$			421	
ν_2 (bend)		1059, 1238	1064, 1225	—	2016
ν_3 (asym)	$\equiv v_{01} \leftarrow v_{00}$	1698	2015	1679	1613
	$v_{02} \leftarrow v_{01}$			1543	
	$v_{03} \leftarrow v_{02}$			1658	
$(2\nu_1)$	$\equiv v_{20} \leftarrow v_{00}$			949	
$(3\nu_1)$	$\equiv v_{30} \leftarrow v_{00}$			1367	
$(\nu_1 + \nu_3)$	$\equiv v_{11} \leftarrow v_{00}$			2293	
$(2\nu_1 + \nu_3)$	$\equiv v_{21} \leftarrow v_{00}$			2881	
$(2\nu_3)$	$\equiv v_{02} \leftarrow v_{00}$			3222	
$(3\nu_1 + \nu_3)$	$\equiv v_{12} \leftarrow v_{00}$			3504	
$(\nu_1 + 2\nu_3)$	$\equiv v_{31} \leftarrow v_{00}$			3761	
$(3\nu_3)$	$\equiv v_{03} \leftarrow v_{00}$			4880	
$(\nu_1 + 3\nu_3)$	$\equiv v_{13} \leftarrow v_{00}$			5431	

[a] UMP2 [83]

[b] 3D MRCI in Jacobi coordinates [95]

Anharmonic bending frequencies (ν_2) can not be calculated from the 2D PES, but harmonic UMP4 bending frequencies, 1059 cm^{-1} and 1238 cm^{-1}, were compared with UMP2 bending frequencies [83], 1064 cm^{-1} and 1225 cm^{-1}, and found both to agree to within 99%. The bending vibration obtained from the 3D MRCI calculations, 2016 cm^{-1}, corresponds to the bending of R_{O-HF} with respect to r_{HF}, as defined in Ref. [95], so the unusually high frequency may be an unreliable number for comparison.

Large discrepancies are also observed in the computed asymmetric stretching $\nu_3(v_{01} \leftarrow v_{00})$ frequencies. Eigenfunctions obtained from a Morse potential fit to UMP2 calculations gives a value ν_3=2015 cm^{-1} [83], almost 300 cm^{-1} higher than the harmonic and anharmonic UMP4 values of 1698 and 1679 cm^{-1}, respectively. The MRCI value, 1613 cm^{-1}, is approximately 50 cm^{-1} lower than the UMP4 values, agreement of 96%. The unusually high UMP2 frequency, 2015 cm^{-1}, may therefore be overestimated.

The spacing between symmetric stretching functions decreases, from 496($= \upsilon_{10} \leftarrow \upsilon_{00}$) cm^{-1} to 450($= \upsilon_{20} \leftarrow \upsilon_{10}$) cm^{-1}, to 421($= \upsilon_{30} \leftarrow \upsilon_{20}$) cm^{-1}, due to anharmonicity. The spacing between the asymmetric stretching eigenfunctions also initially decreases, from 1679($= \upsilon_{01} \leftarrow \upsilon_{00}$) cm^{-1} to 1543($= \upsilon_{02} \leftarrow \upsilon_{01}$) cm^{-1}, but then increases to 1658($= \upsilon_{03} \leftarrow \upsilon_{02}$) cm^{-1}. This mixture of anharmonicity and inverse anharmonicity may arise due to fluctuations in the shape and steepness of the splined 2D PES.

3.3.4 Isotope effects: ODF$^-$

Isotope effects were examined for the heavy isotopomer, ODF$^-$. Twelve low-lying vibrational eigenfunctions and their eigenenergies are shown in Figure 3.11. From the ground state vibrational wave function, υ_{00}, anharmonic O–D and F–D bond lengths $\langle R_{OD} \rangle$ and $\langle R_{FD} \rangle$ could be computed. These values, listed in the last column of Table 3.7, were calculated to be 0.85 Å and 1.10 Å, respectively. Both values are smaller than the corresponding anharmonic OHF$^-$ bond lengths of 1.12 Å and 1.26 Å, respectively, as expected for the heavier isotope with a lower zero-point energy. The UMP4 rotational constant for ODF$^-$, $B = 0.337$ cm^{-1}, is larger than that of OHF$^-$, 0.328 cm^{-1} (see Table 3.8), since the moment of inertia is smaller for the heavier isotopomer with shorter bond lengths. To our knowledge, no experimental value is available for comparison.

The first vibrational overtones of ODF$^-$ are listed in Table 3.10, along with harmonic and anharmonic UMP4 frequencies. The fundamental symmetric and asymmetric stretching frequencies, $\nu_1 = 464(\equiv \upsilon_{10} \leftarrow \upsilon_{00})$ cm^{-1} and $\nu_3 = 1211(\equiv \upsilon_{01} \leftarrow \upsilon_{00})$ cm^{-1}, respectively, of ODF$^-$ are lower than those of OHF$^-$. In general, the heavier isotope generates deeper-lying eigenfunctions than those of its lighter counterpart. The first excited symmetric stretching frequency of ODF$^-$ is 424($\equiv \upsilon_{20} \leftarrow \upsilon_{10}$) cm^{-1}, 32 cm^{-1} lower than that of OHF$^-$. The second excited symmetric stretching frequency, 447($\equiv \upsilon_{30} \leftarrow \upsilon_{20}$) cm^{-1}, demonstrates inverse anharmonicity and is larger than the first overtone. From Figure 3.11, one also can see that whereas the first two symmetric stretching eigenfunctions are dominated by stretching along the R_{DF} bond, the third symmetric stretching eigenfunction, υ_{30}, is slanted in the direction of the R_{OD} coordinate and thus contains asymmetric stretching character as well. This mixing of stretching modes may lead to the observed inverse anharmonicity in the symmetric stretching frequencies.

The isotope effect is even more apparent in the asymmetric stretching frequencies involving the motion of the heavy deuterium between the end atoms. The fundamental

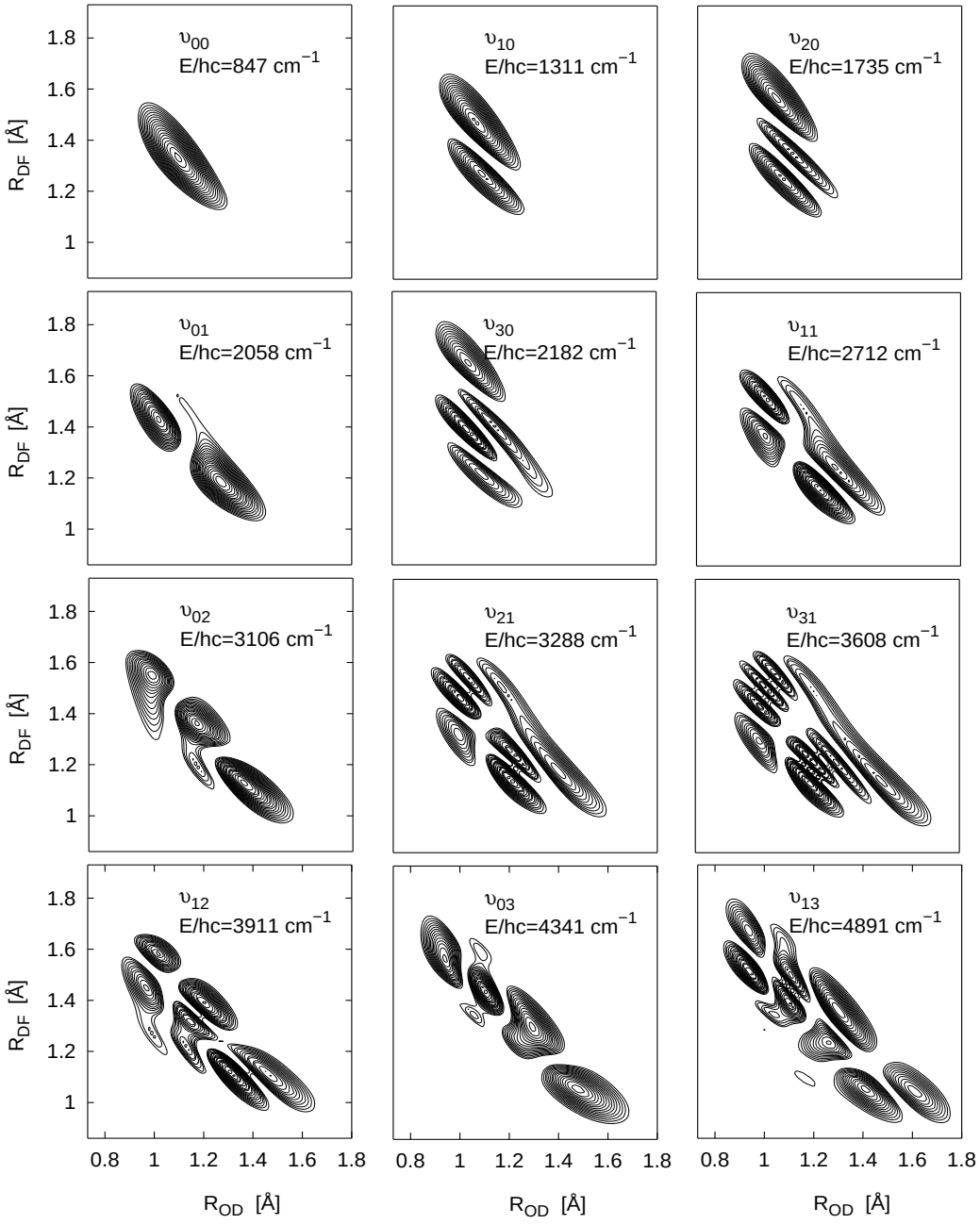

Figure 3.11: 2D anharmonic vibrational eigenfunctions for ODF^-, labelled $\upsilon_{s\,as}$. The symmetric functions ($\upsilon_{s\,0}$) contain nodes perpendicular to the line $R_1 = R_2$, whereas the asymmetric ($\upsilon_{0\,as}$) functions contain nodal planes parallel to the line $R_1 = R_2$. Mixed-mode functions ($\upsilon_{s\,as}$) contain nodes both parallel and perpendicular to the line $R_1 = R_2$. Contours correspond to wave packet density.

and first two excited asymmetric stretching frequencies of ODF^-, 1211($\equiv \upsilon_{01} \leftarrow \upsilon_{00}$) cm^{-1}, 1048($\equiv \upsilon_{02} \leftarrow \upsilon_{01}$) cm^{-1}, and 1235($\equiv \upsilon_{03} \leftarrow \upsilon_{02}$) cm^{-1}, are 468 cm^{-1}, 495 cm^{-1}, and

423 cm^{-1} lower than those of OHF$^-$, respectively. The asymmetric stretching eigenfunctions also demonstrate a mixture of anharmonicity and inverse harmonicity. The spacing between vibrational states initially decreases from 1211($= \upsilon_{01} \leftarrow \upsilon_{00}$) cm^{-1} to 1048($= \upsilon_{02} \leftarrow \upsilon_{01}$) cm^{-1}, and then increases to 1235($= \upsilon_{03} \leftarrow \upsilon_{02}$) cm^{-1}, a pattern similar to that found in OHF$^-$. This mixture of anharmonicity and inverse anharmonicity is attributed to the irregular topology of the 2D PES. Finally, the combination bands listed in Table 3.10 are all lower in energy than the corresponding bands of OHF$^-$ (*cf.* Table 3.9).

Table 3.10: 2D harmonic UMP4 and anharmonic UMP4 vibrational frequencies of ODF$^-$

ODF$^-$		**harmonic** UMP4	**anharmonic** UMP4
Frequency [cm^{-1}]			
ν_1 (sym)	$\equiv \upsilon_{10} \leftarrow \upsilon_{00}$	462	464
	$\upsilon_{20} \leftarrow \upsilon_{10}$		424
	$\upsilon_{30} \leftarrow \upsilon_{20}$		447
ν_2 (bend)		760, 889	—
ν_3 (asym)	$\equiv \upsilon_{01} \leftarrow \upsilon_{00}$	1258	1211
	$\upsilon_{02} \leftarrow \upsilon_{01}$		1048
	$\upsilon_{03} \leftarrow \upsilon_{02}$		1235
$(2\nu_1)$	$\equiv \upsilon_{20} \leftarrow \upsilon_{00}$		888
$(3\nu_1)$	$\equiv \upsilon_{30} \leftarrow \upsilon_{00}$		1335
$(\nu_1 + \nu_3)$	$\equiv \upsilon_{11} \leftarrow \upsilon_{00}$		1865
$(2\nu_3)$	$\equiv \upsilon_{02} \leftarrow \upsilon_{00}$		2259
$(2\nu_1 + \nu_3)$	$\equiv \upsilon_{21} \leftarrow \upsilon_{00}$		2441
$(3\nu_1 + \nu_3)$	$\equiv \upsilon_{31} \leftarrow \upsilon_{00}$		2761
$(\nu_1 + 2\nu_3)$	$\equiv \upsilon_{12} \leftarrow \upsilon_{00}$		3064
$(3\nu_3)$	$\equiv \upsilon_{03} \leftarrow \upsilon_{00}$		3494
$(\nu_1 + 3\nu_3)$	$\equiv \upsilon_{13} \leftarrow \upsilon_{00}$		4044

The ratio of asymmetric stretching frequencies, $\nu_3(\mathrm{OHF}^-)/\nu_3(\mathrm{ODF}^-) = 1.39$, is identical to the predicted ratio from the mass scaling factor for the asymmetric stretch, $\sqrt{(\mu_{as}(\mathrm{ODF}^-)/(\mu_{as}(\mathrm{OHF}^-))}$=1.39. These calculated scaling factors are listed in Table 3.11.

Table 3.11: The scaling factor b for isotopomers OHF^- and ODF^- calculated using the mass of the isomers (m), the reduced mass of the asymmetric stretching vibration (μ_{as}), and the asymmetric stretching frequency, (ν_3).
($*$) Anharmonic frequencies obtained at the UMP4 level of theory.

	scaling factor (b)
$\sqrt{(m_{\mathrm{D}})/(m_{\mathrm{H}})}$	1.41
$\sqrt{(\mu_{as}(\mathrm{ODF}^-)/(\mu_{as}(\mathrm{OHF}^-))}$	1.39
$\nu_3(\mathrm{OHF}^-)/\nu_3(\mathrm{ODF}^-)^{(*)}$	1.39

3.3.5 IR absorption spectra of OHF^- and ODF^-

Finally, we consider the simulated IR absorption spectra of OHF^- and ODF^- to compare absorption intensities and vibrational transition probabilities. The absorption spectra for OHF^- and ODF^- are shown in Figure 3.12; they were calculated in the same manner as the FHF^- spectra (*cf.* Figure 3.6), and over a propagation period of 5 ps. The peak locations and relative intensities are listed in Table 3.12; to the best of our knowledge, no experimental data is available for comparison. Unlike the FHF^- and FDF^- spectra,

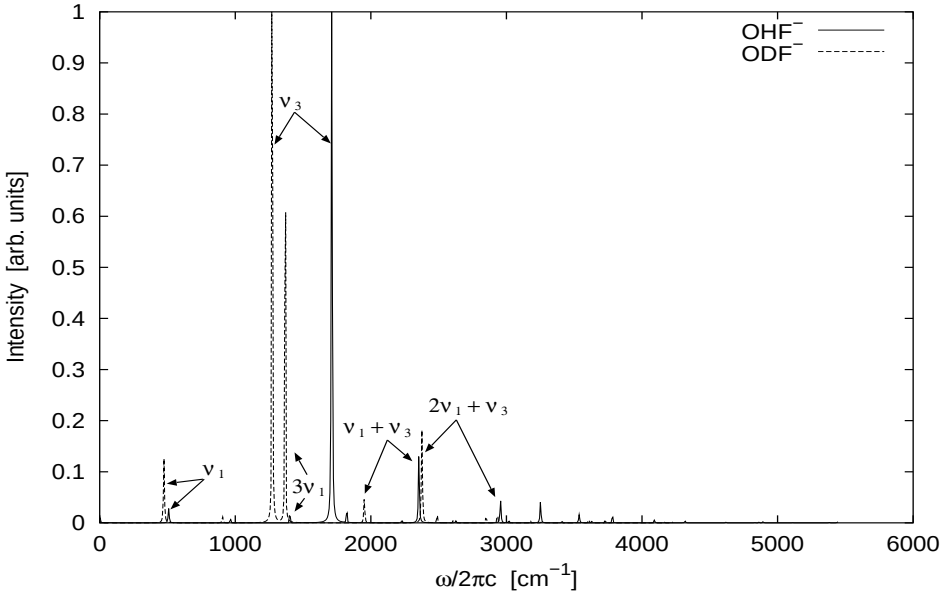

Figure 3.12: Absorption spectra of OHF^- (solid lines) and ODF^- (dashed lines). Vibrational transitions are indicated.

Transition [cm^{-1}]	**OHF$^-$** Absorption spectrum		**ODF$^-$** Absorption spectrum	
	Freq.	Int.	Freq.	Int.
$\nu_1(\equiv \upsilon_{10} \leftarrow \upsilon_{00})$	509	0.03	474	0.13
$\nu_3(\equiv \upsilon_{01} \leftarrow \upsilon_{00})$	1711	1.00	1270	1.00
$3\nu_1(\equiv \upsilon_{30} \leftarrow \upsilon_{00})$	1399	0.01	1371	0.61
$\nu_1 + \nu_3(\equiv \upsilon_{11} \leftarrow \upsilon_{00})$	2354	0.13	1950	0.05
$2\nu_1 + \nu_3(\equiv \upsilon_{21} \leftarrow \upsilon_{00})$	2958	0.04	2377	0.18

Table 3.12: Frequencies and relative intensities of OHF$^-$ and ODF$^-$ IR absorption peaks obtained from theoretical UMP4 calculation.

the OHF$^-$ and ODF$^-$ spectra demonstrate a more complicated structure. In general, the larger number of peaks, as well as the numerous peaks of small intensity (< 0.05), most likely arises due to the asymmetric nature of the molecule and its stretching vibrations. Several low intensity peaks corresponding to vibrational transitions to mixed-mode states are also visible. Unlike in the case of FHF$^-$, the symmetric stretching vibration ν_1 is now IR active since the wave function is no longer symmetric, and it gives rise to low-intensity peaks.

Whereas with FHF$^-$/FDF$^-$, the peaks corresponding to the heavier isotopomer FDF$^-$ are all weaker than those of FHF$^-$, this trend is not observed with OHF$^-$/ODF$^-$. Specifically, ODF$^-$ peaks corresponding to transitions involving more symmetric stretching quanta (ν_1) than asymmetric stretching quanta (ν_3) are more intense than those of OHF$^-$. This phenomenon can be analyzed by comparing the symmetric stretching eigenfunctions of the two isotopomers, *e.g.* υ_{30} (*cf.* Figures 3.10 and 3.11). One sees that υ_{30} of OHF$^-$ is localized along the R_{HF} bond, with almost no mixing with R_{OH}. The wave function υ_{30} of ODF$^-$, on the other hand, is noticeably slanted toward R_{OD}, similar to the behavior of the asymmetric stretching eigenfunctions. In other words, the symmetric stretching eigenfunctions of ODF$^-$ contain more asymmetric stretching character than do the symmetric stretching functions of OHF$^-$. This trend is observed for all ODF$^-$ eigenfunctions containing symmetric stretching quanta. Since the most intense peaks in the absorption spectra of both species are due to the asymmetric stretching vibration, ν_3, one can assume that transitions to states containing asymmetric stretching character are most probable. Therefore, we attribute the intense peaks of ODF$^-$ containing quanta of ν_1 to the asymmetric stretching character of these functions. Let us now continue with a

quantitative analysis of all the absorption peaks.

The peaks of highest relative intensity (1.00) correspond to the asymmetric stretching vibration $\nu_3(\equiv \upsilon_{01} \leftarrow \upsilon_{00})$ for ODF^- at 1270 cm^{-1} (dashed), and for OHF^- at 1711 cm^{-1} (solid). The medium intensity (0.61) peak at 1371 cm^{-1} belonging to ODF^- is due to a transition from υ_{00} to the third excited symmetric stretching eigenstate, υ_{30}, which also contains asymmetric stretching character (see Figure 3.11). The corresponding peak $(\upsilon_{30} \leftarrow \upsilon_{00})$ for OHF^- is located at 1399 cm^{-1} and has a very weak relative intensity of 0.01, most likely since it contains less asymmetric stretching character (see Figure 3.10). The medium (0.13) intensity peak at 2354 cm^{-1}, belonging to OHF^- (solid), can be assigned to the combination band $\nu_1 + \nu_3(\equiv \upsilon_{11} \leftarrow \upsilon_{00})$, and the corresponding peak for ODF^- is located 404 cm^{-1} lower at 1950 cm^{-1}, with a relative intensity 0.05. The peak at 2377 cm^{-1} belonging to ODF^- (dashed), 0.18 relative intensity, is assigned to the transition $2\nu_1 + \nu_3(\equiv \upsilon_{21} \leftarrow \upsilon_{00})$, and the corresponding peak for OHF^- (solid) is located 581 cm^{-1} higher at 2958 cm^{-1} with relative intensity of 0.04. Finally, the low intensity peaks near 500 cm^{-1} correspond to the first symmetric stretching frequency, $\nu_1(\equiv \upsilon_{10} \leftarrow \upsilon_{00})$, and are calculated to be 474 cm^{-1}, with relative intensity 0.13 for ODF^- (dashed) and 509 cm^{-1}, with relative intensity 0.03, for OHF^- (solid).